



Technical Note

Cloud Phase Recognition Based on Oxygen A Band and CO₂ 1.6 μm Band

Qinghui Li , Xuejin Sun * and Xiaolei Wang

College of Meteorology and Oceanography, National University of Defense Technology, Changsha 410000, China; liqinghui@nudt.edu.cn (Q.L.); wangxiaolei@nudt.edu.cn (X.W.)

* Correspondence: xuejin.s@nudt.edu.cn

Abstract: The accurate recognition of the cloud phase has a great influence on the retrieval of the cloud top height. In order to improve the accuracy of obtaining the cloud top height with OCO-2, we proposed a cloud phase recognition algorithm based on the threshold of parameter α ; α is defined as the reflectivity ratio of the region with weak continuous absorption of the oxygen A band to the region with weak continuous absorption of the CO₂ 1.6 μm band. The α under different solar zenith angles and different ground albedos was calculated. The results show the following: under the same surface albedo and solar zenith angle, α was large for ice clouds and small for water clouds. Under the same surface albedo, the greater the solar zenith angle, the smaller the α of the ice cloud, and the larger the α of the water cloud. Under the same solar zenith angle, the greater the surface albedo, the smaller the α ; when the solar zenith angle was less than 70°, α can be used to effectively distinguish between the ice cloud and water cloud. This study used OCO-2 data of a single orbit over ocean to verify the feasibility of the algorithm through comparison with the CALIOP cloud phase product, which provided a basis for OCO-2 cloud top height estimation.

Keywords: cloud phase; OCO-2; threshold method; O₂-A band; CO₂ 1.6 μm band



Citation: Li, Q.; Sun, X.; Wang, X. Cloud Phase Recognition Based on Oxygen A Band and CO₂ 1.6 μm Band. *Remote Sens.* **2021**, *13*, 1681. <https://doi.org/10.3390/rs13091681>

Academic Editor: Tamas Várnai

Received: 14 March 2021

Accepted: 24 April 2021

Published: 27 April 2021

Publisher's Note: MDPI stays neutral with regard to jurisdictional claims in published maps and institutional affiliations.



Copyright: © 2021 by the authors. Licensee MDPI, Basel, Switzerland. This article is an open access article distributed under the terms and conditions of the Creative Commons Attribution (CC BY) license (<https://creativecommons.org/licenses/by/4.0/>).

1. Introduction

Clouds consist of droplets, ice crystals, or a mixture of both, which are visible aggregates floating in the air formed by the condensation of water vapor in the atmosphere. Clouds are an important part of the atmosphere. Clouds exist in more than half of the sky on the earth at any time [1]. The thermodynamic and dynamic processes accompanying the cloud phase change process affect the formation and evolution of the weather system [2,3]. Clouds affect the water cycle of the atmosphere through the precipitation process, and at the same time have an important impact on the earth's radiation budget [4–7]. The fifth IPCC report pointed out that the radiation effect of clouds is among the most uncertain factors in evaluating future climate development and evolution [8,9]. The radiation effect of clouds mainly depends on the nature of clouds, such as the cloud top height, cloud optical thickness (COT), cloud phase, and particle size; among them, the cloud phase significantly affects the planet's radiation balance [10–12], and the accurate identification of cloud phase is an important prerequisite for measuring cloud parameters, such as cloud optical thickness and particle size [13]. Therefore, the accurate identification of cloud phase state is an important basic work in satellite remote sensing.

The recognition of cloud phase is mainly based on the difference between the optical and physical properties of ice cloud and water cloud [14]. The use of infrared bands to identify cloud phase has been in development for a long time. This basic principle is based on the differences in the absorption rates of water-phase particles and ice-phase particles in certain infrared bands. Ackerman et al. [15] proposed a three-band cloud phase recognition method based on 8, 11, and 12 μm. After that, Strabala et al. [16] further established a cloud phase recognition algorithm for 8.5, 11, and 12 μm. Later, the algorithm simplified to the dual-channel algorithm of 8.5 μm and 11 μm was applied to MODIS [14],

but the recognition capability is limited for optically thin cirrus and clouds with cloud top temperatures between 250 and 265 K [14,17]. To solve this problem, Baum et al. used three pairs of channels of 7.3 $\mu\text{m}/11 \mu\text{m}$, 8.5 $\mu\text{m}/11 \mu\text{m}$, and 11 $\mu\text{m}/12 \mu\text{m}$, and combined a near-infrared channel for cloud phase recognition [14,18]. Nasiri et al. [19] found that AIRS observations at 960 cm^{-1} and 1231 cm^{-1} channels are more sensitive to phase states. On the basis of Nasiri's research, Jin et al. [17] proposed a fast-computing cloud phase recognition algorithm for AIRS and simulated a brightness temperature of 700 to 1300 cm^{-1} for single-layer water and ice clouds. This algorithm set a threshold of brightness temperature and three thresholds of brightness temperature difference for cloud phase recognition. Since the upper layer or upper part of the opaque cloud contributes more to the measurement of AIRS, the main goal of the AIRS cloud phase recognition algorithm is to identify more ice clouds. Later, Jin et al. [13] used CALIPSO to evaluate the cloud phase recognition capability of AIRS. The recognition result of AIRS on the ice cloud is consistent with that of CALIPSO, but the recognition capability of the water cloud is poor. Cloud phase recognition algorithms based entirely on infrared bands can be applied to day and night scenes, but these methods are sensitive to water vapor absorption, which will cause errors in cloud phase recognition.

In addition to infrared bands, near-infrared bands can also be used to identify cloud phases [20,21]. The essence of identifying cloud phases on the basis of solar reflectivity is the difference in absorption characteristics between liquid water droplets and ice crystal particles at 1.6, 2.1, or 3.7 μm [13]. Pilewskie et al. [22] used the reflectivity of the 1.65 μm channel for cloud phase recognition. Key et al. [20] used AVHRR's 3.75 μm channel to obtain cloud phases of the Arctic region. Arking et al. [23] used AVHRR's 0.6, 3.7, and 11 μm channels to study cloud phase recognition. Knap et al. [24] used the threshold parameter S1.67 to identify the cloud phase, which is defined as the ratio of the difference between the spectral reflectivities at 1.70 and 1.64 μm to the reflectivity at 1.64 μm , and used an airborne visible and infrared imaging spectrometer (AVIRIS) measurement to verify the effectiveness of the algorithm. Miller et al. [25] used the characteristics of the 1.6 and 2.5 μm channels to detect the mixed phase cloud of supercooled water droplets above the ice cloud, and then Wang et al. [26] used these two channels to study the recognition of cloud phases.

The CALIOP mounted on CALIPSO recognizes the cloud phase on the basis of the depolarization ratio [27]. CALIPSO can provide accurate vertical cross-sections of the cloud phase and measure the distribution of ice and water in the optically thin cloud [28]. Cho et al. [29] and Jin et al. [13] evaluated the cloud phase products of MODIS and AIRS using the cloud phase products of CALIOP, respectively.

OCO-2 is a satellite dedicated to the study of carbon dioxide in the atmosphere. The accuracy, resolution, and coverage of the CO_2 data obtained by OCO-2 can satisfy the characteristics of CO_2 sources and sinks and seasonal periodic changes of CO_2 on a regional scale. At present, the OCO-2 satellite only processes the clear sky area data when estimating CO_2 and does not process it when there are clouds. The oxygen A band hyperspectral data observed by OCO-2 can be used to retrieve the cloud top height, but it is necessary to accurately distinguish the cloud phase; there are currently few cloud phase recognition algorithms for OCO-2. Richardson et al. [30] used OCO-2 to obtain the geometric thickness of low-level water clouds on the sea surface and proposed a method to identify cloud phase states by using the radiance of the oxygen A band and CO_2 1.6 μm band (CO_2 weak absorption band) after the zenith correction but did not specifically analyze the recognition capability of this method.

Therefore, on the basis of the channel characteristics of OCO-2, this paper analyzed the hyperspectral radiation characteristics of different types of clouds in the oxygen A band and the CO_2 weak absorption band, and proposes a cloud phase recognition algorithm based on the thresholding of parameter α . We used the CALIOP cloud phase product of a single orbit to compare and verify, which proved the effectiveness of the algorithm.

2. Data and Method

2.1. Data

This paper used OCO-2 to identify cloud phase, using OCO-2's L1bsc and CALIPSO's VFM data. OCO-2 is NASA's first dedicated carbon dioxide monitoring satellite. It operates in a sun-synchronous orbit, with an orbital height of 705 km, an orbital inclination of 98.2°, a repetition period of 16 days for the ground trajectory, and 13:30 at the ascending node. It belongs to the A-train satellite sequence. OCO-2 is equipped with 3 common-view imaging grating spectrometers, which collect a high-resolution sunlight-reflected spectrum in the molecular oxygen (O₂) A band around the center wavelength of 765 nm and the CO₂ band around 1610 and 2060 nm.

VFM data are a cloud phase product that can provide the vertical structure and cloud type data of the cloud layer below 30 km. CALIPSO is a sun-synchronous satellite with a revisit period of 16 days, and its equator crossing time is 13:30 local time. The laser wavelength of the CALIOP lidar is 532 and 1064 nm, which can detect optical thin cirrus clouds with an optical thickness of 0.01 or less. OCO-2 and CALIPSO both belong to the A-train satellite sequence, which is very convenient for data matching and result verification.

2.2. Method

In this paper, the radiation transmission mode software package SCIATRAN developed by the Institute of Environmental Physics/Remote Sensing Institute of the University of Bremen was used for radiation transmission simulations [31,32]. SCIATRAN can solve a variety of scientific problems in atmospheric radiation simulations and is widely used at present [33–35]. The SCIATRAN cloud parameterization scheme can set the cloud type, cloud height, cloud optical thickness, effective particle radius, cloud water path, etc. All simulations in this article were carried out in a plane parallel atmosphere. The atmospheric model was set as the mid-latitude summer standard atmosphere model, the observation zenith angle was 0°, the spectral resolution was 0.04 nm, and the cloud thickness was 1 km; the water droplet radius was set to 12 μm, and the ice particle was a hexagonal prism with a side length of 50 μm and a height of 100 μm.

The recognition of cloud phase depends on the differences in the optical and micro-physical properties of the ice cloud and water cloud. In the oxygen A band and CO₂ weak absorption band, due to (i) the difference in the scattering phase function (the backscattering of ice crystals is greater than that of water droplets), the reflectivity of the ice cloud in the O₂ A band is greater, and (ii) the imaginary part of the refractive index and the particle size of ice cloud are both larger than those of the water cloud, which causes the absorption of the ice cloud in the weak CO₂ absorption band to be stronger than that of the water cloud. Therefore, the radiation characteristics of the ice cloud and water cloud are significantly different; thus, the oxygen A band and the CO₂ weak absorption band can be combined for cloud phase recognition. Figure 1 shows the reflected spectral radiance of the ice cloud and water cloud with a surface albedo of 0.02, a cloud top height of 4 km, and an optical thickness of 10. It can be seen from Figure 1a that under the same cloud top height and the same optical thickness, the reflected spectral radiance of the ice cloud in the oxygen A band was greater than that of the water cloud. It can be seen from Figure 1b that in the CO₂ weak absorption band, the radiance of ice clouds was lower than that of water clouds.

The radiance spectra of the oxygen A band and CO₂ weak absorption band were affected not only by the cloud phase but also by the cloud top height and optical thickness.

The radiance of the oxygen A band and CO₂ weak absorption band was simulated when the optical thicknesses were 1, 2, 5, 10, 20, and 40; the cloud top height of the ice cloud was 9 km; and the cloud top height of the water cloud was 4 km. The ratio of the spectral radiance of different optical thicknesses to the spectral radiance of the optical thickness of 1 is shown in Figure 2, where the subscript of I represents the optical thickness. It can be seen from Figure 2 that the optical thickness had a great influence on the radiance. As the optical thickness increased, the radiance of the ice cloud and water cloud in the oxygen

A band and the CO₂ weak absorption band generally increased, and the growth rate of radiance for the water cloud was greater than that for the ice cloud.

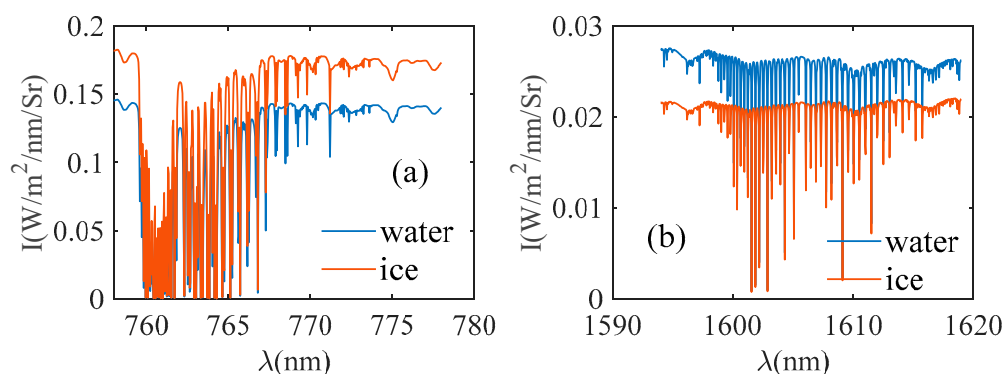


Figure 1. Reflected spectral radiance of ice cloud and water cloud in the oxygen A band and CO₂ weak absorption band under the same cloud top height and the same optical thickness. (a) Oxygen A band; (b) CO₂ weak absorption band.

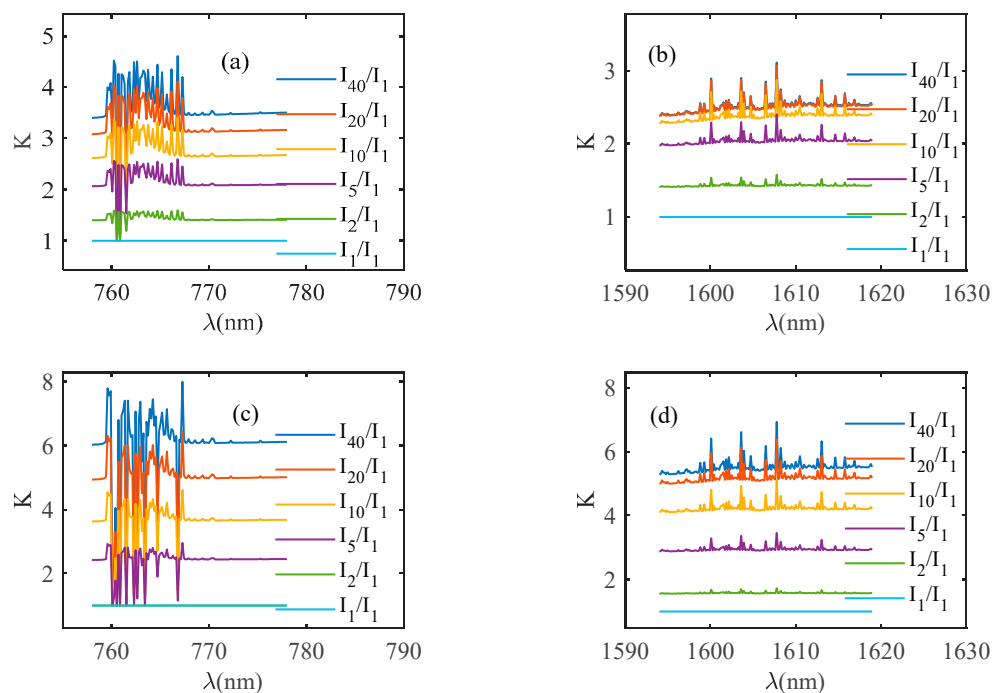


Figure 2. The ratio of the radiance of ice cloud and water cloud in oxygen A band and CO₂ weak absorption band under different optical thicknesses. (a,b) are ice cloud. (c,d) are water cloud.

The radiance of the oxygen A band and CO₂ weak absorption band was simulated when the optical thickness was 10; the cloud top heights of the ice cloud were 9, 10, 11, and 15 km, and the cloud top heights of the water cloud were 2, 3, 4, and 8 km. Figure 3 shows the ratio of the spectral radiance of different cloud top heights to the spectral radiance of 9 km in the ice cloud and the ratio of the spectral radiance of different cloud top heights to the spectral radiance of cloud tops of 2 km in the water cloud, where the subscript of I represents the cloud top height.

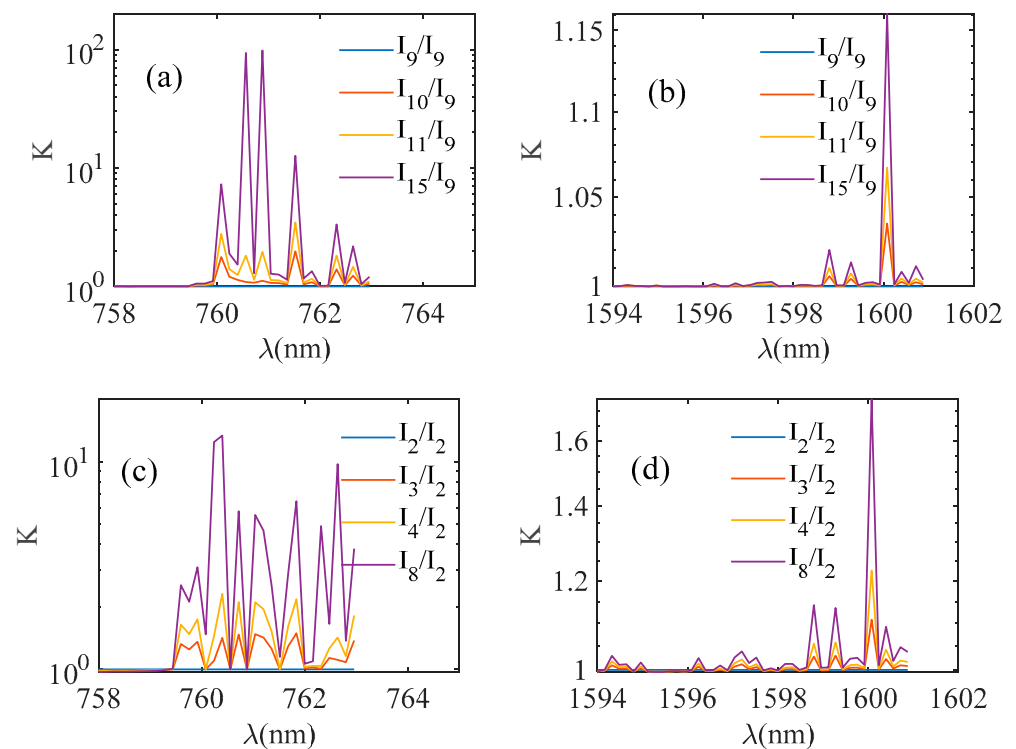


Figure 3. The ratio of the radiance of ice cloud and water cloud in oxygen A band and CO₂ weak absorption band at different cloud top heights. (a,b) are ice cloud. (c,d) are water cloud.

Both the oxygen A band and the CO₂ weak absorption band are gas absorption bands. The radiance of the region with absorption is greatly affected by cloud top height, and it is difficult to reflect the cloud phase information. Therefore, in order to reduce or eliminate the influence of cloud top height when performing cloud phase recognition, one should select the regions with minimal gas absorption.

It can be seen from Figure 3 that the height of the cloud top had little effect on the radiance of the region with weak continuous absorption in oxygen A band (758–759 nm) and the region with weak continuous absorption in CO₂ weak absorption band (1594–1595 nm). Since the region with weak continuous absorption of oxygen A band and CO₂ weak absorption band were less affected by the cloud top height, we chose these two regions for cloud phase recognition.

The reflectivity of the region with weak continuous absorption in oxygen A band is denoted as R_{O_2} , and the reflectivity of the region with weak continuous absorption in CO₂ weak absorption band is denoted as R_{CO_2} , and their ratio is denoted as α , as shown in Equation (1); the spectral reflectivity R is defined as Equation (2), where L_λ is the reflected spectral radiance, S_λ is spectral solar irradiance, and θ is the solar zenith angle.

$$\alpha = \frac{R_{O_2}}{R_{CO_2}} \quad (1)$$

$$R_\lambda = \frac{\pi L_\lambda}{S_\lambda \cos \theta} \quad (2)$$

Figure 4 shows the scatter plot of α versus R_{O_2} of the ice cloud and water cloud of different cloud heights and different optical thicknesses with a surface albedo of 0.02 and variation of R_{O_2} with optical thickness. The cloud top heights of ice cloud were 9, 10, 11, and 15 km; the cloud top heights of the water cloud were 2, 3, 4, and 8 km; the solar zenith angle (SZA) was 30°; the observation zenith angle was 0°; and the optical thicknesses were 0.1, 0.2, 0.5, 1, 2, 5, 10, 20, 40, and 80.

It can be seen from Figure 4 that R_{O_2} had a positive correlation with optical thickness; therefore, R_{O_2} can reflect the size of COT. With the same optical thickness, the α of ice cloud with different cloud top heights hardly changed, and the change in the α of water cloud was also small; therefore, the influence of the change in cloud top height on α could be ignored. The α of ice cloud continued to increase with the increase in R_{O_2} ; when R_{O_2} was less than 0.2, the α of water cloud decreased with the increase in R_{O_2} , and when R_{O_2} was greater than 0.2, it increased with the increase in R_{O_2} . When R_{O_2} was the same, the α of the ice cloud was greater than that of the water cloud; therefore, the cloud phase can be judged jointly by α and R_{O_2} (see Figure 4d).

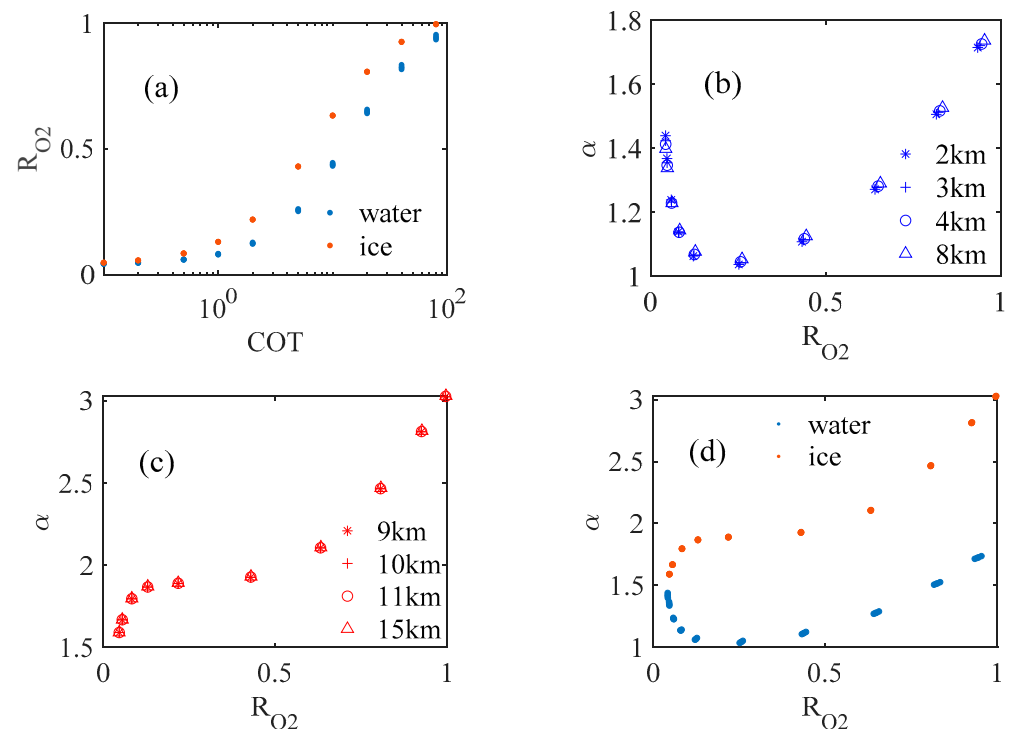


Figure 4. The change in R_{O_2} with optical thickness and the change in α with R_{O_2} (a). The change in R_{O_2} with optical thickness (b). The change in α with R_{O_2} of water cloud in different cloud top heights (c). The change in α with R_{O_2} of ice cloud in different cloud top heights (d). Comparison of α of ice cloud and water cloud at different cloud top heights and different optical thicknesses.

3. Results

3.1. The Influence of the Solar Zenith Angle on α

Figure 5 shows the variation of α with R_{O_2} when the surface albedo was 0.02 and the solar zenith angles were 30° and 70° . Among them, the cloud top heights of ice cloud were 9, 10, 11, and 15 km; the cloud top heights of water cloud were 2, 3, 4, and 8 km; and the optical thicknesses were 0.1, 0.2, 0.5, 1, 2, 5, 10, 20, 40, and 80. It can be seen from Figure 5 that, as the solar zenith angle increased, the α of the ice cloud decreased at the same R_{O_2} , and the α of the water cloud increased. When the solar zenith angle was 30° , the α of the ice cloud was obviously larger than that of the water cloud; when the solar zenith angle was 70° , and when R_{O_2} was small—that is, when the optical thickness of the cloud layer was small—the α of ice cloud was smaller than the water cloud, but the α of the ice cloud was larger than the water cloud as a whole.

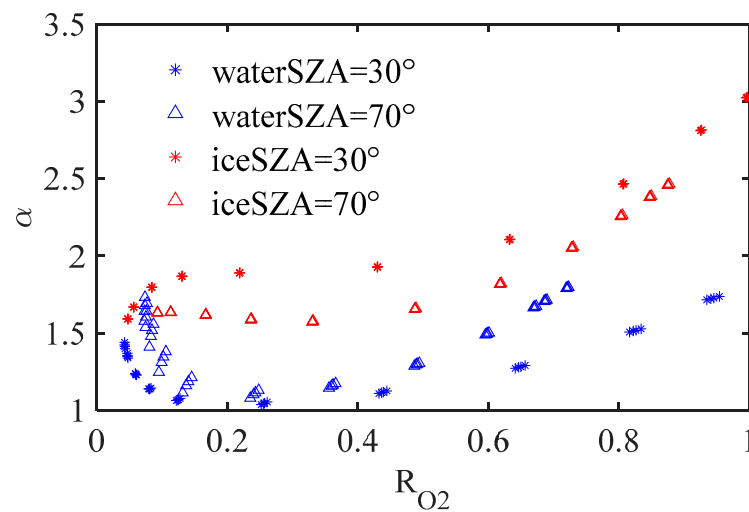


Figure 5. Comparison of α of ice cloud and water cloud under different solar zenith angles.

3.2. The Influence of Surface Albedo on α

Figure 6 shows the variation of α with R_{O_2} when the surface albedos were 0.02 and 0.3, and the solar zenith angles were 30° and 70° . Among them, the cloud top heights of ice cloud were 9, 10, 11, and 15 km; the cloud top heights of water cloud were 2, 3, 4, and 8 km; and the optical thicknesses were 0.1, 0.2, 0.5, 1, 2, 5, 10, 20, 40, and 80. It can be seen from Figure 6 that for the same solar zenith angle, cloud optical thickness, and cloud top height, for a given value of R_{O_2} , the values of α were smaller for a larger surface albedo. However, when R_{O_2} was large, that is, when the cloud was optically thick, α was hardly affected by surface albedo.

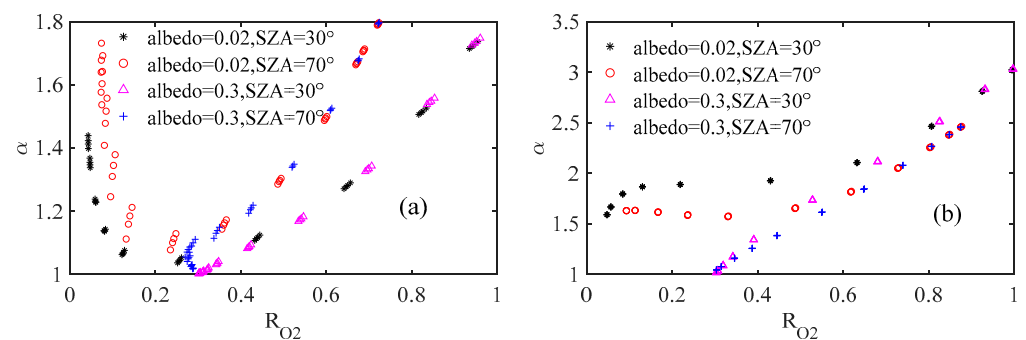


Figure 6. Variation of α with R_{O_2} under different surface albedos: (a) water cloud; (b) ice cloud.

When the surface albedo was 0.3, the α of ice cloud and water cloud is shown in Figure 7. It can be seen from Figure 7 that the α of ice cloud and water cloud changed greatly compared to surface albedo of 0.02. Even when the optical thickness was very small, R_{O_2} was still around 0.3, which was close to the surface albedo. At this time, the contribution of the reflected radiance mainly came from the surface, and it was difficult to identify the cloud phase. Therefore, the greater the surface albedo, the more difficult it was to identify optically thin cloud.

It can be seen from the above research that the change in α with R_{O_2} was related to the solar zenith angle and the surface albedo. Through the simulation of α under different solar zenith angles and surface albedos, we could see that when the solar zenith angle was less than 70° , the ice cloud and water cloud could be effectively distinguished by α , but it was difficult to distinguish when the optical thickness was small. The surface albedo had an effect on α ; therefore, the threshold α was different under different surface albedos.

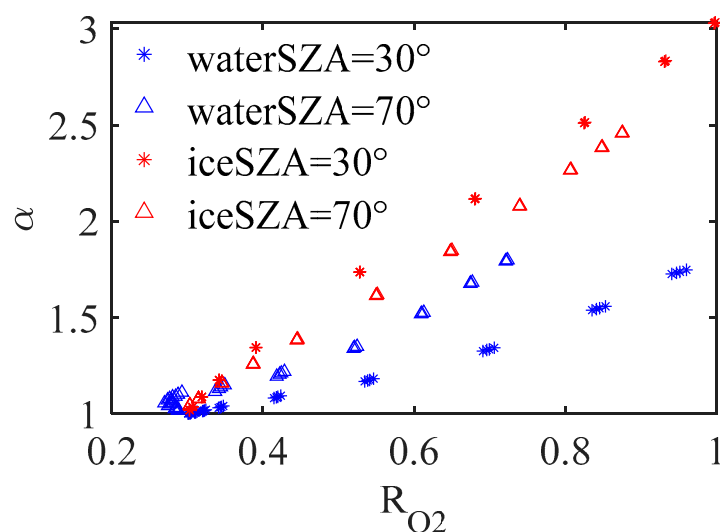


Figure 7. The α of ice cloud and water cloud when the surface albedo was 0.3.

Before performing cloud phase recognition, one must judge whether there are clouds in the sky. The OCO-2 data in August 2016 was used for comparison with the CALIOP data. The samples selected according to latitude and longitude were from the 450 orbits during August 2016 over the Pacific Ocean. The latitude was between -60° and 60° , and the solar zenith angle was less than 70° . The change in $\mu^{-1}I_{WKCO_2}$ with $\mu^{-1}I_{O_2}$ is shown in Figure 8; μ is $\cos(\text{SZA})$; I_{O_2} and I_{WKCO_2} are continuum radiances of the oxygen A band and CO_2 weak absorption band, respectively. As shown in Figure 8, when there were no clouds, $\mu^{-1}I_{WKCO_2}$ and $\mu^{-1}I_{O_2}$ were small; therefore, the threshold of $\mu^{-1}I_{WKCO_2}$ and $\mu^{-1}I_{O_2}$ can be set to determine whether there are clouds. When $\mu^{-1}I_{WKCO_2}$ and $\mu^{-1}I_{O_2}$ were both less than the threshold, it was judged as no clouds; otherwise, it was judged as yes. The judgment accuracy rate was defined as the proportion of cloud or no cloud distinguished by the threshold to the total cloud or no cloud. The variation of the judgment accuracy rate with the set threshold is shown in Figure 9.

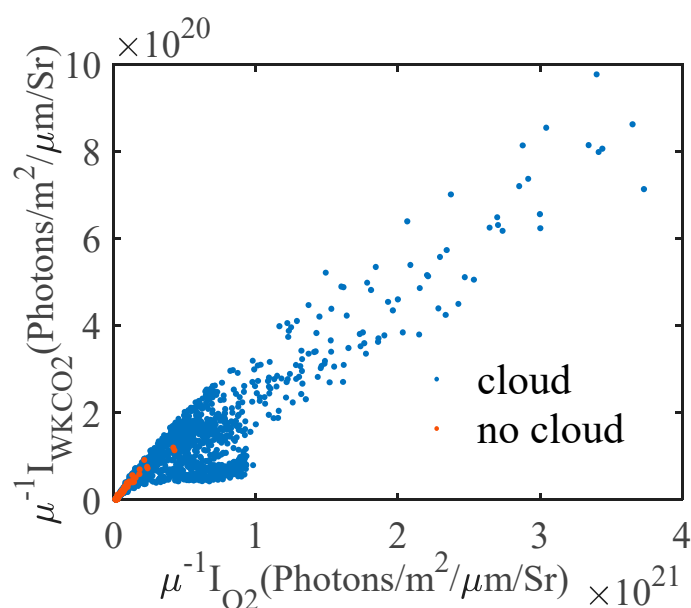


Figure 8. $\mu^{-1}I_{WKCO_2}$ varied with $\mu^{-1}I_{O_2}$.

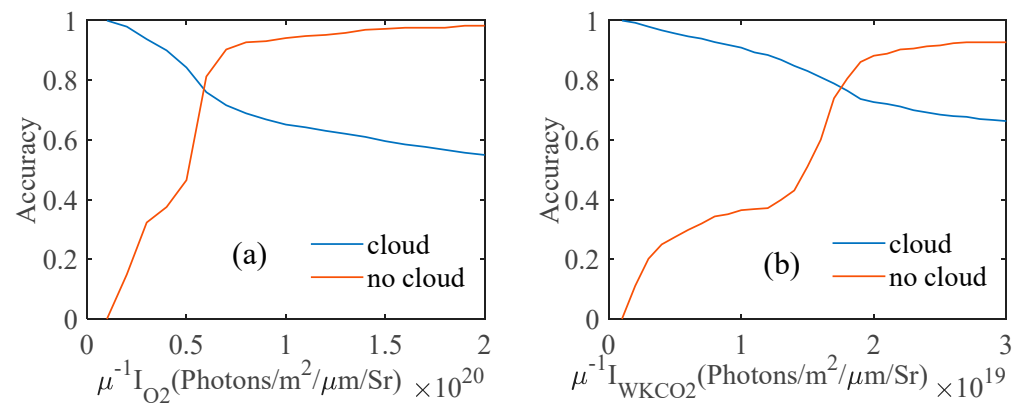


Figure 9. The judgment accuracy rate of cloud and no cloud varied with the threshold. (a) Accuracy varied with $\mu^{-1}I_{O_2}$. (b) Accuracy varied with $\mu^{-1}I_{WKCO_2}$.

As shown in Figure 9, as $\mu^{-1}I_{WKCO_2}$ and $\mu^{-1}I_{O_2}$ increased, the accuracy of judging cloudiness decreased, and the accuracy of judging cloudlessness increased. We set the thresholds of $\mu^{-1}I_{WKCO_2}$ and $\mu^{-1}I_{O_2}$ to 1.8×10^{19} Photons $m^{-2}s^{-1}\mu m^{-1}$ and 6×10^{19} Photons $m^{-2}s^{-1}\mu m^{-1}$, respectively, and the accuracy of the discrimination between cloud and no cloud at this time was 79.60% and 79.17%.

As shown in Figure 10, using the same OCO-2 data as Figure 8 to calculate α , combined with the cloud phase results of the monolayer cloud provided by CALIOP, we calculated the changes of α with R_{O_2} , and then, respectively, fit the changes of α with R_{O_2} for the ice cloud and water cloud. The R^2 of the ice cloud fitting curve and water cloud fitting curve were 0.8631 and 0.6968, respectively; then, we took the middle line of the two fitting curves as the threshold curve for cloud phase recognition. At this time, the probability that the ice cloud was distributed above the threshold curve was 92.67%, and the probability of water cloud distribution below the threshold curve was 77.19%.

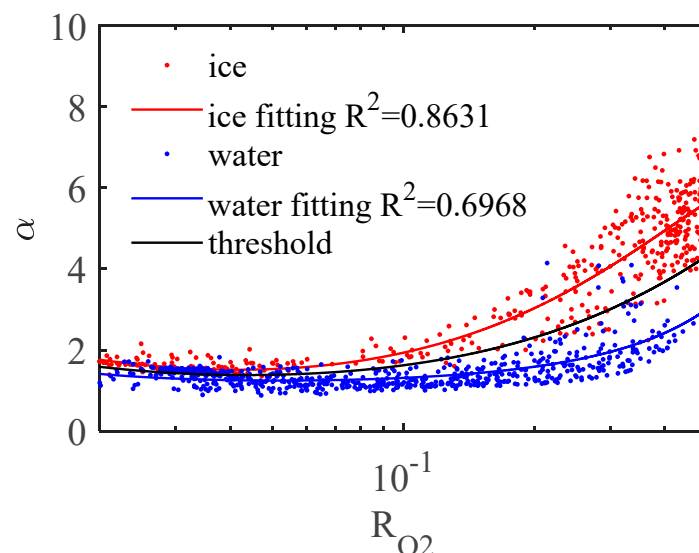


Figure 10. The variation in α with R_{O_2} of the measured data of OCO-2.

When using OCO-2 data for cloud phase recognition, we first judged whether there were clouds or not. If $\mu^{-1}I_{O_2}$ and $\mu^{-1}I_{WKCO_2}$ were both less than the threshold given above, we judged it as unknown or not determined, and the rest were judged as clouds. After that, we used OCO-2 data to calculate α and R_{O_2} . When α was above the threshold curve, it was judged to be ice cloud; otherwise, it was judged to be water cloud.

The OCO-2 data of track 5778 on 3 August 2015, which was located over the Pacific, were used for cloud phase recognition, and the recognition result and the CALIOP cloud phase product are shown in Figure 11. Figure 11a is the result of the cloud phase product of CALIOP; Figure 11b is the result of the cloud phase recognition obtained by the OCO-2 data using the threshold method.

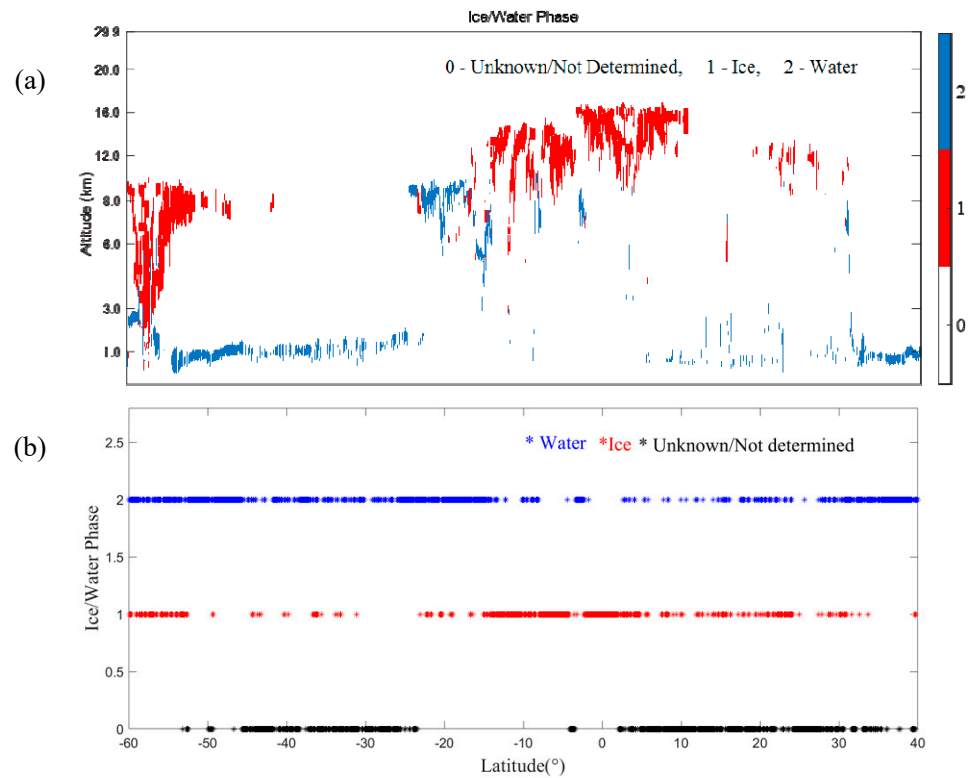


Figure 11. Comparison of cloud phase recognition results. (a) CALIOP. (b) OCO-2.

4. Discussion

The variation in α with R_{O_2} of the recognition result shown in Figure 11 is shown in Figure 12. Figure 13 shows the quantitative analysis results of cloud phase recognition on the basis of the threshold method.

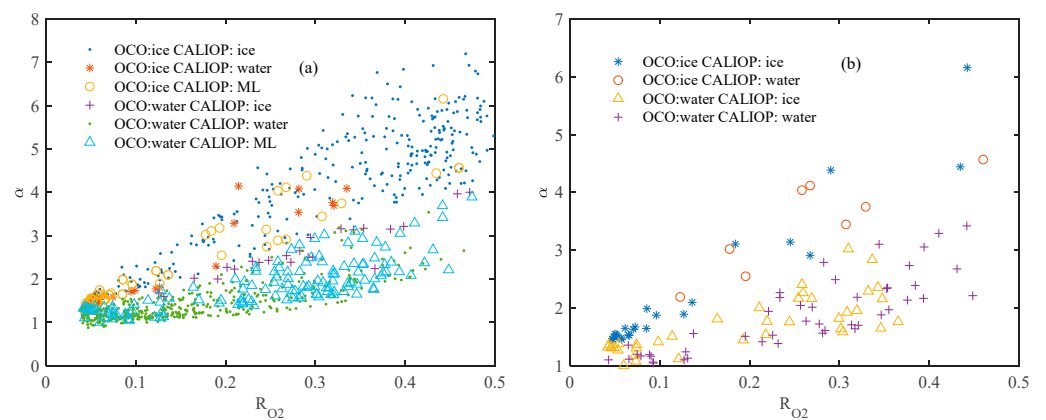


Figure 12. The variation of cloud phase recognition results: (a) OCO-2 recognition results and different CALIOP cloud products; (b) OCO-2 recognition results and CALIOP multi-layer cloud with different top clouds.

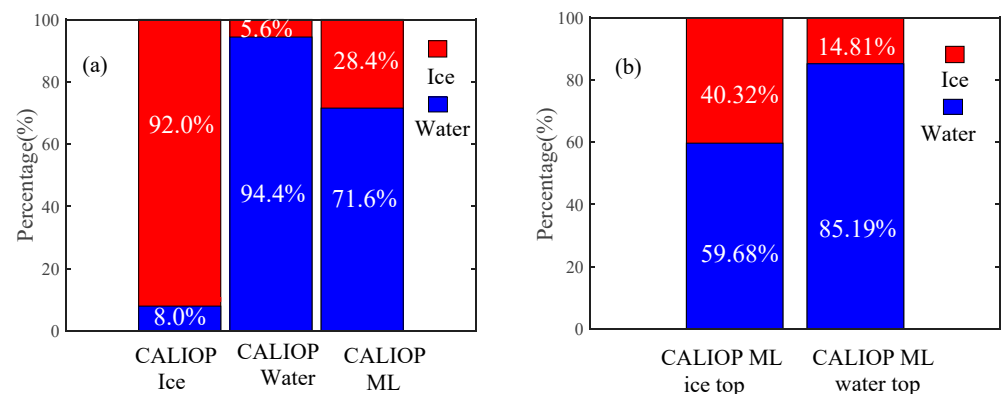


Figure 13. Quantitative analysis results of cloud phase recognition. (a) Compared with the CALIOP cloud phase product, our algorithm judges the percentage of ice cloud and water cloud. The abscissa “CALIOP Ice” represents ice cloud, “CALIOP Water” represents water cloud, and “CALIOP ML” represents multi-layer cloud. (b) When CALIOP is identified as a multi-layer cloud, compared with the CALIOP cloud phase product, our algorithm judges the percentage of ice cloud and water cloud. The abscissa “CALIOP ML, ice top” represents multi-layer cloud whose top cloud is ice cloud; “CALIOP ML, water top” represents multi-layer cloud whose top cloud is water cloud.

As shown in Figures 12 and 13, for single-layer cloud, the recognition rate of ice cloud was 92%, and the recognition rate of water cloud was 94.4%, achieving a high recognition rate. The probability of the multi-layer cloud being identified as the water cloud was higher than that of the ice cloud. For the multi-layer cloud whose top cloud was water cloud, the probability of being recognized as water cloud was 85.19%. For the multi-layer cloud whose top cloud was ice cloud, the probability of being recognized as ice cloud was 40.32%. When the top cloud of the multi-layer cloud was a water cloud, it was mainly identified as water cloud, but when the top cloud of the multi-layer cloud was ice cloud, the probability of the ice cloud and the water cloud in the recognition result was not much different. In conjunction with Figure 12, it can be seen that there was no significant difference between the variation of α with the R_{O_2} of the multi-layer cloud and single-layer cloud. Therefore, this algorithm is not suitable for cloud phase recognition of a multi-layer cloud.

5. Conclusions

The accurate recognition of cloud phase has a great influence on the cloud top height retrieved by satellite remote sensing. In order to improve the accuracy of using OCO-2 to obtain the cloud top height, we carried out a study of cloud phase recognition, and the cloud phase recognition algorithm based on threshold of reflectance ratio α was proposed. Simulations show that (1) under the same surface albedo and solar zenith angle, the α of the ice cloud was large, the α of the water cloud was small, and α increased with the increase in reflectivity of the region with weak continuous absorption in the oxygen A band; (2) under the same surface albedo, the larger the solar zenith angle, the smaller the α of the ice cloud, and the larger the α of the water cloud; (3) under the same solar zenith angle, the greater the surface albedo, the smaller the α ; (4) when the solar zenith angle was less than 70° , the ice cloud and water cloud could be effectively distinguished by α . This paper used OCO-2 data over the ocean for verification, and the comparison with CALIOP cloud phase product data showed that they had high recognition capability. However, the OCO-2 data used for verification belonged to a single orbit. The evaluation will need to use a dataset that is statistically representative of a wide range of locations and seasons.

The cloud phase recognition algorithm in this paper is not suitable for the recognition of the phase of the uppermost cloud layer of multi-layer cloud. The next step is to combine multiple channels to distinguish between multi-layer clouds and single-layer clouds.

In addition to OCO-2, Japan’s GOSAT and China’s TANSAT both contain the oxygen A band and CO_2 weak absorption band. Therefore, the algorithm can be widely used.

Author Contributions: All authors were involved in the design and discussion of the study. This research idea was conceived by X.S. and Q.L. The experiments were designed and conducted by Q.L. The data were analyzed and interpreted by Q.L. The manuscript was written by Q.L. and revised by X.S. and X.W. All authors have read and agreed to the published version of the manuscript.

Funding: This study was financially supported by the National Natural Science Foundation of China (NSFC) (grant no. 41575020).

Data Availability Statement: In this manuscript, we used two kinds of data, the VFM data of CALIPSO ("https://asdc.larc.nasa.gov/data/CALIPSO/LID_L2_VFM-Standard-V4-20" (accessed on 13 January 2021)) and the L1bsc data of OCO-2 ("<https://disc.gsfc.nasa.gov/datasets?page=1&subject=Infrared%20Wavelengths&measurement=Infrared%20Radiance&project=OCO-2>" (accessed on 13 January 2021)).

Conflicts of Interest: The authors declare no conflict of interest.

References

1. Kuze, A.; Chance, K.V. Analysis of cloud top height and cloud coverage from satellites using the O₂ A and B bands. *J. Geophys. Res. Atmos.* **1994**, *99*, 14481–14491. [[CrossRef](#)]
2. Liou, K.N. Influence of Cirrus Clouds on Weather and Climate Processes: A Global Perspective. *Mon. Weather Rev.* **1986**, *114*, 1167. [[CrossRef](#)]
3. Li, J.; Yi, Y.; Minnis, P.; Huang, J.; Yan, H.; Ma, Y.; Wang, W.; Ayers, J.K. Radiative effect differences between multi-layered and single-layer clouds derived from CERES, CALIPSO, and CloudSat data. *J. Quant. Spectrosc. Radiat. Transf.* **2011**, *112*, 361–375. [[CrossRef](#)]
4. Wetherald, R.T. Cloud Feedback Processes in a General Circulation Model. *J. Atmos.* **1988**, *45*, 1397–1416. [[CrossRef](#)]
5. Baker, M.B.; Peter, T. Small-scale cloud processes and climate. *Nature* **2008**, *451*, 299–300. [[CrossRef](#)]
6. Trenberth, K.E.; Fasullo, J.T.; Kiehl, J. Earth's Global Energy Budget. *Bull. Am. Meteorol. Soc.* **2009**, *90*, 311–323. [[CrossRef](#)]
7. Dessler, A.E. A Determination of the Cloud Feedback from Climate Variations over the Past Decade. *Science* **2010**, *330*, 1523–1527. [[CrossRef](#)] [[PubMed](#)]
8. Wang, H.; Su, W. Evaluating and understanding top of the atmosphere cloud radiative effects in Intergovernmental Panel on Climate Change (IPCC) Fifth Assessment Report (AR5) Coupled Model Intercomparison Project Phase 5 (CMIP5) models using satellite observations. *J. Geophys. Res. Atmos.* **2013**, *118*, 683–699. [[CrossRef](#)]
9. Stocker, T.; Plattner, G.K.; Dahe, Q. IPCC Climate Change 2013: The Physical Science Basis-Findings and Lessons Learned. In *Egu General Assembly Conference*; IPCC: Genève, Switzerland, 2014.
10. Ackerman, T.; Valero, F.; Liou, K. Heating rates in tropical anvils. *J. Atmos. Sci.* **1986**, *45*, 1606–1623. [[CrossRef](#)]
11. Hartmann, D.; Ockert-Bell, M.; Michelsen, M. The Effect of Cloud Type on Earth's Energy Balance: Global Analysis. *J. Clim.* **1992**, *5*, 1281–1304. [[CrossRef](#)]
12. Mcfarquhar, G.M.; Cober, S.G. Single-Scattering Properties of Mixed-Phase Arctic Clouds at Solar Wavelengths: Impacts on Radiative Transfer. *J. Clim.* **2004**, *17*, 3799–3813. [[CrossRef](#)]
13. Jin, H.; Nasiri, S.L. Evaluation of AIRS cloud-thermodynamic-phase determination with CALIPSO. *J. Appl. Meteorol. Climatol.* **2014**, *53*, 1012–1027. [[CrossRef](#)]
14. Baum, B.A.; Menzel, W.P.; Frey, R.A.; Tobin, D.C.; Ping, Y. MODIS Cloud-Top Property Refinements for Collection 6. *J. Appl. Meteorol. Clim.* **2012**, *51*, 1145–1163. [[CrossRef](#)]
15. Ackerman, S.A.; Smith, W.L.; Revercomb, H.E.; Spinhirne, J.D. The 27 28 October 1986 FIRE IFO Cirrus Case Study: Spectral Properties of Cirrus Clouds in the 8 12 μm Window. *Mon. Weather Rev.* **1990**, *118*, 2377–2388. [[CrossRef](#)]
16. Strabala, K.I.; Ackerman, S.A.; Menzel, W.P. Cloud properties inferred from 8-12 μm data. *J. Appl. Meteorol.* **1994**, *33*, 212–229. [[CrossRef](#)]
17. Jin, H. Satellite Remote Sensing of Mid-Level Clouds. Satellite Remote Sensing of Mid-Level Clouds. Ph.D. Thesis, Texas A&M University, College Station, TX, USA, 2012.
18. Platnick, S.; King, M.D.; Ackerman, S.A.; Menzel, W.P.; Baum, B.A.; Riédi, J.C.; Frey, R.A. The MODIS cloud products: Algorithms and examples from Terra. *IEEE Trans. Geosci. Remote Sens.* **2003**, *41*, 459–473. [[CrossRef](#)]
19. Nasiri, S.L.; Kahn, B.H. Limitations of Bispectral Infrared Cloud Phase Determination and Potential for Improvement. *J. Appl. Meteorol. Clim.* **2007**, *47*, 2895–2910. [[CrossRef](#)]
20. Key, J.R.; Intrieri, J.M. Cloud Particle Phase Determination with the AVHRR. *J. Appl. Meteorol.* **2000**, *39*, 1797–1804. [[CrossRef](#)]
21. Daniel, J.S. Cloud liquid water and ice measurements from spectrally resolved near-infrared observations: A new technique. *J. Geophys. Res. Atmos.* **2002**, *107*, AAC 21-1–AAC 21-16. [[CrossRef](#)]
22. Pilewskie, P.; Twomey, S. Cloud Phase Discrimination by Reflectance Measurements near 1.6 and 2.2 μm . *J. Atmos. Sci.* **1987**, *44*, 3419–3420. [[CrossRef](#)]
23. Arking, A.; Childs, J.D. Retrieval of Cloud Cover Parameters from Multispectral Satellite Images. *J. Appl. Meteorol.* **2003**, *24*, 322–333. [[CrossRef](#)]

24. Knap, W.H.; Stammes, P.; Koelemeijer, R.B.A. Cloud Thermodynamic-Phase Determination From Near-Infrared Spectra of Reflected Sunlight. *J. Atmos. Sci.* **2002**, *59*, 83–96. [[CrossRef](#)]
25. Miller, S.D. Liquid-top mixed-phase cloud detection from shortwave-infrared satellite radiometer observations: A physical basis. *J. Geophys. Res. Atmos.* **2014**, *119*, 8245–8267. [[CrossRef](#)]
26. Wang, J.; Liu, C.; Min, M.; Hu, X.; Lu, Q.; Husi, L. Effects and Applications of Satellite Radiometer 2.25- μm Channel on Cloud Property Retrievals. *IEEE Trans. Geosci. Remote Sens.* **2018**, *56*, 5207–5216. [[CrossRef](#)]
27. CALIPSO/CALIOP cloud phase discrimination algorithms. *J. Atmos. Ocean. Technol.* **2009**, *26*, 2293–2309. [[CrossRef](#)]
28. Winker, D.M.; Vaughan, M.A.; Omar, A.; Hu, Y.; Powell, K.A.; Liu, Z.; Hunt, W.H.; Young, S.A. Overview of the CALIPSO Mission and CALIOP Data Processing Algorithms. *J. Atmos. Ocean. Technol.* **2009**, *26*, 2310–2323. [[CrossRef](#)]
29. Cho, H.M.; Nasiri, S.L.; Yang, P.; Laszlo, I.; Zhao, X.T. Application of CALIOP measurements to the evaluation of cloud phase derived from MODIS infrared channels. *J. Appl. Meteorol. Clim.* **2009**, *48*, 2169–2180. [[CrossRef](#)]
30. Richardson, M.; Leinonen, J.; Cronk, H.Q.; McDuffie, J.; Stephens, G.L. Marine liquid cloud geometric thickness retrieved from OCO-2's oxygen A-band spectrometer. *Atmos. Meas. Tech.* **2019**, *12*, 1717–1737. [[CrossRef](#)]
31. Rozanov, A.; Rozanov, V.; Buchwitz, M.; Kokhanovsky, A.; Burrows, J.P. SCIATRAN 2.0—A new radiative transfer model for geophysical applications in the 175–2400nm spectral region. *Adv. Space Res.* **2005**, *36*, 1015–1019. [[CrossRef](#)]
32. Pohl, C.; Rozanov, V.V.; Mei, L.; Burrows, J.P.; Spreen, G. Implementation of an ice crystal single-scattering property database in the radiative transfer model SCIATRAN. *J. Quant. Spectrosc. Radiat. Transf.* **2020**, *253*, 107118. [[CrossRef](#)]
33. Eichmann, K.U.; Weber, M.; Heue, K.P.; Leventiduo, E.; Richter, A.; Burrows, J.P. Tropical Upper Tropospheric Ozone Volume Mixing Ratios Retrieved with the Cloud Slicing Method using SCIATRAN/GOME2 data: Methodology, Ozone Sonde Comparisons, and Verification of the new S-5P Operational Processor. In *Esa Living Planet Symposium*; European Space Agency: Prague, Czech Republic, 2016.
34. Li, Y.; Zhang, C.; Wang, D.; Chen, J.; Liu, D.; Rong, P. Comparison between the ESFT method and LBL method of CO₂ retrieval for high-resolution satellite. In *Proceedings of SPIE-The International Society for Optical Engineering*; International Society for Optics and Photonics: Bellingham, DC, USA, 2015; Volume 9449.
35. Liu, D.; Zhang, C.; Li, Y.; Rong, P. The influence of temperature on the simulated high resolution spectra of enhanced SCIATRAN model in near infrared band. *Opt. Int. J. Light Electron Opt.* **2016**, *127*, 7292–7299. [[CrossRef](#)]